

3D-UIR: 3D Gaussian for Underwater 3D Scene Reconstruction via Physics-Based Appearance-Medium Decoupling

Jieyu Yuan, Yujun Li, Yuanlin Zhang, Chunle Guo, Xiongxin Tang,
Ruixing Wang, and Chongyi Li, *Senior Member, IEEE*

Abstract—Novel view synthesis for underwater scene reconstruction presents unique challenges due to complex light-media interactions. Optical scattering and absorption in water body bring inhomogeneous medium attenuation interference that disrupts conventional volume rendering assumptions of uniform propagation medium. While 3D Gaussian Splatting (3DGS) offers real-time rendering capabilities, it struggles with underwater inhomogeneous environments where scattering media introduce artifacts and inconsistent appearance. In this study, we propose a physics-based framework that disentangles object appearance from water medium effects through tailored Gaussian modeling. Our approach introduces appearance embeddings, which are explicit medium representations for backscatter and attenuation, enhancing scene consistency. In addition, we propose a distance-guided optimization strategy that leverages pseudo-depth maps as supervision with depth regularization and scale penalty terms to improve geometric fidelity. By integrating the proposed appearance and medium modeling components via an underwater imaging model, our approach achieves both high-quality novel view synthesis and physically accurate scene restoration. Experiments demonstrate our significant improvements in rendering quality and restoration accuracy over existing methods. The project page is available at <https://bilityniu.github.io/3D-UIR>.

Index Terms—Underwater image, novel view synthesis, image restoration, appearance decoupling.

I. INTRODUCTION

UNDERWATER optical images are crucial for marine information capture, as their rich textures and accessibility make them indispensable for a wide range of underwater vision applications [1]–[3]. Despite these advantages, planar 2D imaging inherently suffers from limited spatial information representation, which is insufficient for the precision modeling and advanced analytical requirements of modern marine applications. The transition from 2D imagery to volumetric 3D models enables substantially richer geometric characterization and spatial context in underwater 3D reconstruction [4], making it a key technology for marine mapping, underwater

archaeology, environmental monitoring, and autonomous underwater vehicle navigation. Multi-view imagery enables precise spatial analysis of underwater environments [5], enabling enhanced scene comprehension in stereoscopic 3D space to support more complex task requirements.

Unlike clear-air environments, underwater scenes present unique optical challenges due to complex light-medium interactions. Specifically, light propagation through water involves wavelength-dependent attenuation and particle scattering [8]–[10], resulting in depth-dependent color distortion and visibility degradation [11]. These optical phenomena result in both forward and backward scattering effects, creating veiling light and spatial blur that significantly degrade underwater image quality. The physical constraints of underwater environments alter image formation, introducing greenish or bluish color casts and blurred backgrounds that pose challenges for general scene reconstruction methods. Consequently, underwater degradation fundamentally disrupts the photometric consistency assumptions essential for multi-view 3D reconstruction.

Underwater environments’ unique optical properties challenge existing volume rendering-based view synthesis methods, which typically assume light transport involves only emission and absorption while neglecting underwater scattering and attenuation effects. While recent advances in volume rendering-based approaches, including implicit neural fields [12] and explicit representations [6], have demonstrated remarkable success in general scenes, they face fundamental limitations in underwater environments. Specifically, the alpha blending algorithm typically assumes that radiance along viewing rays is modulated solely by emission and absorption [6], [12], [13], ignoring complex light transport characteristics of participating media. In contrast, in underwater scenarios, the water medium itself actively participates in the imaging process through continuous scattering and attenuation, introducing translucent effects absent in clear-air rendering [14]. This creates **two key challenges**: **1) Medium Veiling Opacity**: the volumetric nature of water as a participating medium induces continuous scattering events along light paths, resulting in depth-dependent veiling effects that cannot be accurately represented through standard opacity accumulation models [15]. **2) View-Dependent Inconsistency**: The depth-dependent attenuation leads to significant appearance variations across different viewpoints, violating the assumption of consistent scene radiance that the same 3D point should exhibit consistent intrinsic radiance properties regardless of viewing angle [16]. This assumption underlies existing methods. These physical constraints manifest as reconstruction artifacts such as water-cloud floats, color inconsistencies,

Jieyu Yuan and Yujun Li are with the VCIP, College of Computer Science, Nankai University, Tianjin 300350, China (e-mail: jieyuyuan.cn@gmail.com; 2111903@mail.nankai.edu.cn).

Yuanlin Zhang is with the VCIP, College of Computer Science, Nankai University, Tianjin 300350, China, and also with the Institute of Software, Chinese Academy of Sciences, Beijing 100190, China (e-mail: zason_zyl@163.com).

Xiongxin Tang is with the Institute of Software, Chinese Academy of Sciences, Beijing 100190, China (e-mail: xiongxin@iscas.ac.cn).

Ruixing Wang is with DJI, Shenzhen 518000, China (e-mail: ruixingw@hustuniqu.com).

Chunle Guo and Chongyi Li are with the VCIP, College of Computer Science, Nankai University, Tianjin 300350, China, and also with the Nankai International Advanced Research Institute (NKIARI), Shenzhen Futian, China (e-mail: guochunle@nankai.edu.cn; lichongyi@nankai.edu.cn).

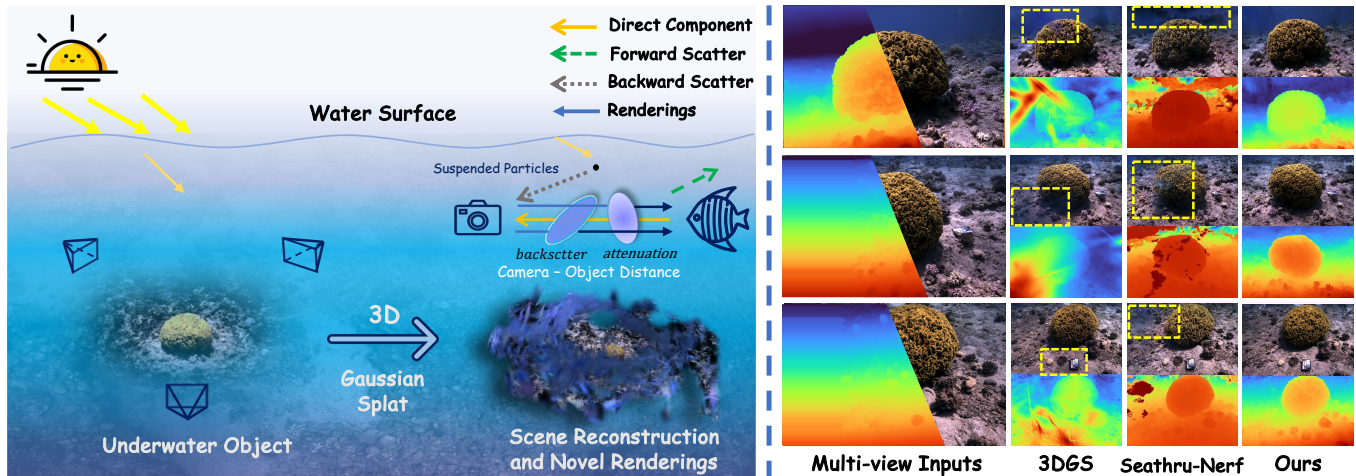


Fig. 1. Optical scattering and absorption in underwater environments present unique challenges for novel view synthesis. The standard volume rendering equation inadequately models participating media with suspended particles, resulting in the incorrect reconstruction of volumetric water as the floating artifacts in 3D representation (left). Additionally, light source directionality and viewing angles cause attenuation variations that result in inconsistent scene appearance across viewpoints (right). 3DGS [6] lacks proper modeling of scattering media, causing water column effects on scene surfaces and resulting in collapsed depth representations. Existing scattering Novel View Synthesis (NVS) methods, e.g., SeaThru-NerF [7], fail to account for dynamic photometric variations, which introduces water float artifacts (highlighted in yellow boxes). In contrast, our approach effectively models the participating medium to render photorealistic novel views with accurate scene representation, yielding more consistent scene rendering across novel viewpoints and effective elimination of underwater artifacts.

and inadequate modeling of the translucent properties of the medium, significantly compromising the fidelity of synthesized novel views in underwater environments, as illustrated in Fig. 1. To solve these challenges, existing scattering-aware novel view synthesis methods [15], [17]–[19] primarily model media representation while overlooking the unique attenuation properties of underwater environments that cause inconsistent scene radiance. Such limitations result in view-dependent artifacts and distance-induced depth collapse, as shown in the right panel of Fig. 1, progressively impairing reconstruction quality with changing perspectives and range. Therefore, the unique optical properties of the medium necessitate that specialized disentangling of object appearance from medium-induced distortions is crucial for accurate and consistent view synthesis under underwater conditions.

In this study, we propose a physics-based underwater scene reconstruction framework that explicitly models the complex light transport characteristics in underwater environments. Our approach employs a 3D Gaussian representation to decompose underwater scenes by separating intrinsic scene properties from water-induced effects, where the object appearance captures the true colors and textures while the medium appearance models the scattering and attenuation caused by water. Specifically, we model the underwater medium by independently representing physics-driven components and integrating them via the image formation model, bypassing the complexity of implicit network estimation. For object appearance, we associate Gaussian primitives with a learned embedding space that captures camera-specific variation, allowing the embedding to modulate Gaussian properties and mitigate view-dependent effects from wavelength-dependent attenuation. Furthermore, to enhance reconstruction accuracy, we incorporate depth-guided optimization using pseudo-depth maps, which significantly improves the precision of underwater image formation

model solutions. We also introduce a specialized Gaussian flattening constraint that mitigates occlusion artifacts caused by incorrectly reconstructed water media. This comprehensive approach not only enables high-fidelity rendering of novel underwater viewpoints but also allows for scene restoration by parametrically removing water medium effects.

In summary, we make the following contributions:

- **Decoupled Underwater Representation:** We propose a physics-based underwater 3DGS representation that decouples object appearance from water medium effects, explicitly modeling complex light transport in participating media while removing water float artifacts caused by translucent scattering media.
- **Consistent Scene Restoration:** We propose an underwater appearance model that combines object and medium appearance representations, enabling consistent scene reconstruction under varying underwater conditions and wavelength-dependent attenuation. Additionally, a pixel-based while balance technique is incorporated to achieve optimal color balance while preventing oversaturation in the restored scene.
- **Distance Guided Optimization:** We propose a distance optimization strategy that improves scene distance estimation accuracy, leading to more precise water-object parameter estimation and reduced volumetric artifacts. This strategy ensures both high-quality geometric representation and physically accurate scene restoration.

The remainder of the paper is organized as follows. In Section II, we present the background of novel view synthesis and underwater scene representation. Section III introduces the preliminaries, covering both 3D Gaussian splatting and the underwater image formation model. Section IV details our methodology. In Section V, we conduct comprehensive experiments to evaluate our method and perform ablation

studies to validate key components. Section VI concludes the paper.

II. RELATED WORK

A. Novel View Synthesis

Novel View Synthesis generates arbitrary views of a scene from limited 2D images. Neural Radiance Field (NeRF) [12] maps color and density to an implicit function, enabling high-quality rendering through volume rendering [12], [20], [21]. In contrast, 3D Gaussian Splatting (3DGS) [6] uses explicit representations, achieving superior real-time performance by representing scene points as Gaussian primitives with a differentiable tile-based rasterizer [6], [22], [23]. While both methods achieve high-fidelity reconstructions [17], [24]–[26], they struggle in scenarios with inconsistent scene density and radiance, often leading to ghosting and artifacts in unconstrained image collections [16], [27]. To address this issue, recent works model inconsistent components separately. For example, NeRF-W [16] introduces per-image latent appearance embeddings to decompose scenes into image-dependent and shared components. SWAG [27] extends appearance modeling by modulating Gaussian colors and constructing image-dependent opacity variations. Similarly, GS-W [28] leverages distinct intrinsic and dynamic appearance features for complex scenes. Underwater scenes share similarities with “in-the-wild” scenes in terms of medium-object interactions. Inspired by appearance modeling techniques for variable scene conditions, we propose a novel approach that incorporates latent appearance modeling to separately represent object and scattering medium characteristics, integrating an underwater physical imaging model to improve reconstruction consistency.

B. Underwater Scene Representation

Underwater scene representation requires joint modeling of scene geometry and medium properties, with attenuation effects already extensively studied in 2D representation. Underwater image restoration focuses on recovering visual perception from degraded images [29]–[31]. Current approaches fall into two categories: direct image enhancement methods that process pixels to improve contrast, saturation, and sharpness [32]–[36], and inverse methods based on Underwater Image Formation Model (UIFM) [37] that estimates attenuation coefficients to recover images [38]–[42]. While physical-based models can produce realistic results with accurate parameters, single-image approaches require prior assumptions for parameter estimation due to the ill-posed nature of this problem [15].

In contrast, 3D reconstruction with multiple views effectively constrains this ill-posed problem and improves parameter estimation accuracy [43], making UIFM-based methods particularly suitable for underwater scene reconstruction. SeaThru-NeRF [7] incorporates scattering media modeling within the rendering equation, separating direct and backscatter components to enhance scene reconstruction. WaterHE-NeRF [44] proposes a novel water ray-tracing field that encodes color, density, and illumination attenuation in 3D space based on Retinex theory. Recent works [19], [45], [46] explore real-time modeling of underwater scattering media using the

high-performance capabilities of 3DGS. WaterSplatting [18] employs GS for explicit geometry representation and a separate volumetric field for capturing the scattering medium. UW-GS [47] introduces a physics-based density control strategy to enhance the clarity of distant objects and employs a binary motion mask to eliminate shadow-like artifacts. Aquatic-GS [48] constructs the Neural Water Field to obtain the underwater coefficients, while introducing a depth-guided optimization mechanism for better distance estimation. Different from the above approaches, they rely primarily on MLP-based implicit estimation of medium parameters through the UIFM, which are constrained by training and rendering speed limitations. In contrast, our method leverages explicit depth-guided scattering media modeling with joint depth optimization during training. Our method balances computational efficiency and physical accuracy, offering significant improvements in underwater scene reconstruction.

III. PRELIMINARIES

A. 3D Gaussian Splatting

3DGS [6] is an explicit representation technique that offers efficient high-quality rendering with real-time performance. The method initializes 3D Gaussians from Structure-from-Motion (SfM) [49] points, transforming them into volumetric primitives that are projected onto 2D space. Each 3D Gaussian is defined as:

$$G(x - \mu, \Sigma) = \exp\left(-\frac{1}{2}(x - \mu)^T \Sigma^{-1}(x - \mu)\right), \quad (1)$$

where $\mu \in \mathbb{R}^3$ is the center position of the Gaussian points, Σ is a 3D covariance matrix that represents the shape, scale, and orientation characteristics of the Gaussian primitives in 3D space. To ensure Σ remains positive semi-definite during optimization, it is factorized into a rotation quaternion $\in \mathbb{R}^4$ and a scaling factor $\in \mathbb{R}^3$:

$$\Sigma = R S S^T R^T. \quad (2)$$

3DGS employs a tile-based rasterizer to efficiently render the scene by projecting all Gaussians onto the image plane. Each Gaussian carries additional attributes, including opacity (α) and color (c), with color represented using third-order spherical harmonic coefficients to model view-dependent appearance. The final color for each pixel is computed through α -blending by accumulating the contributions from overlapping 2D Gaussians:

$$C = \sum_{i \in G_r} c_i \sigma_i \prod_{j=1}^{i-1} (1 - \sigma_j), \quad (3)$$

$$\sigma_i = G_r(px' - \mu_i, \Sigma'_i), \quad (4)$$

where r represents the position of a pixel and G_r denotes the sorted Gaussian points associated with that pixel. Similarly, depth maps are rendered by accumulating the depth values d_i of ordered Gaussian primitives along each ray:

$$D = \sum_{i \in n_i} d_i \alpha_i \prod_{j=1}^{i-1} (1 - \alpha_j). \quad (5)$$

All Gaussian attributes are optimized through the differentiable rasterizer. To enhance representation quality, 3DGS dynamically adapts the scene geometry by periodically splitting large Gaussians with high gradient values and duplicating smaller ones, ensuring efficient and high-fidelity scene reconstruction.

B. Underwater Image Formation Model

Underwater imagery suffers from degradation due to scattering and absorption during light propagation, introducing attenuation and backscatter effects that impair information representation [10]. The captured image I intensity combines two components: direct object radiance traveling to the observer and backscatter from all directions along the light path. Following the revised underwater image formation model [15], [37], the scene captured along line-of-sight distance z is expressed as:

$$I = J \cdot e^{-\beta^D \cdot z} + B^\infty \cdot (1 - e^{-\beta^B \cdot z}), \quad (6)$$

where J is the unattenuated image from the ideal clear scene and B^∞ is the value of backscatter at infinite distance. Here, β^D and β^B are the attenuation coefficients for direct and backscatter components, respectively. UIFM assumes objects are opaque while the medium is semi-transparent with constant low density [37]. This distinction enables separate modeling of backscatter effects and object radiance. However, in neural representations, direct light reflection and translucent media often appear ambiguous when modeled as Gaussian primitives [13], [50]. To address this challenge, our method separately models objects and media, computing attenuation parameters based on UIFM to enhance underwater scene reconstruction quality.

IV. METHODOLOGY

Underwater scattering medium poses significant challenges to conventional 3D GS, introducing volumetric artifacts and compromising scene consistency due to complex light interactions and depth-dependent attenuation that varies across viewpoints. We propose a physics-based method to address these challenges.

Our approach begins with multi-view underwater images processed through COLMAP [49] for Gaussian primitive initialization. After creating 3D Gaussians, Underwater Appearance Modeling (UAM) encodes appearance features, view embeddings by camera pose through an MLP that applies affine color transformations. These per-Gaussian colors undergo 2D projection and tile-based rasterization to generate an initial scene appearance representation. At the same time, Scatter Medium Modeling (SMM) estimates view-specific backscatter and attenuation parameters based on the projected scene depth information. The integration of these branches occurs in the IFM-based rendering stage, where clean scene colors from the projection step serve as input to our Underwater Image Formation Model (UIFM). The UIFM combines these colors with the medium parameters estimated by the SMD branch through physics-based α -blending, transforming clean rendered colors into degraded underwater images that match

the photometric characteristics of captured underwater images for training supervision. Additionally, the Depth-guided Regularization Optimization (DRO) provides pseudo-depth supervision to improve parameter estimation accuracy. During training, Adaptive Density Control dynamically manages Gaussian distribution through cloning, pruning, and strategic addition of primitives, which helps balance scene fidelity and computational efficiency. The complete framework is illustrated in Fig. 2.

A. Underwater Appearance Modeling

Underwater imagery suffers from distance-dependent attenuation causing inconsistent colors and photometric variations across viewpoints, which severely compromises both novel view synthesis and scene restoration quality. To address these issues, we introduce an underwater appearance modeling framework. By leveraging specialized per-Gaussian appearance embeddings, our method effectively captures local variations and mitigates view-dependent color distortions inherent to the underwater medium. We adopt an adaptive affine color transformation that explicitly models view-specific conditions. Specifically, for the i -th Gaussian primitive observed from viewing direction \mathbf{r} , we parameterize the transformation using channel-wise scaling and offset factors $(\beta, \gamma) = \{(\beta_k, \gamma_k)\}_{k=1}^3$ for each color channel k :

$$\tilde{c}_i = \gamma \cdot \hat{c}_i(\mathbf{r}) + \beta, \quad (7)$$

where $\hat{c}_i(\mathbf{r})$ represents the view-dependent base color and \tilde{c}_i denotes the transformed result.

In-the-wild scene, NVS methods [16], [27], [28] employ trainable per-image index embeddings to represent appearance variations. During inference, these methods require ground truth images, often using one half for appearance matching while evaluating metrics on the other half. However, this reliance on per-input view supervision poses a fundamental limitation for underwater environments, where training viewpoints are significantly sparser than the novel view requirements. To overcome this limitation, we construct appearance embeddings from camera poses, exploiting the insight that camera parameters optimized through global bundle adjustment adhere to a consistent maximum a posteriori probability distribution [51]. This formulation enables effective generalization to novel viewpoints without requiring training on the test set. We implement this approach through a tiny MLP (two-layer MLP with 128 hidden units) that projects camera parameters into a low-dimensional appearance latent space to capture the underlying probabilistic distribution of these poses:

$$\mathbf{e}_i = \text{MLP}(\gamma\{\mathbf{R}, \mathbf{t}\}), \quad (8)$$

where $\gamma\{\cdot\}$ denotes positional encoding, and \mathbf{R} and \mathbf{t} correspond to the rotation matrix and translation vector of the camera pose, respectively.

To further enhance appearance consistency while preserving spatial coherence, we associate each Gaussian with an appearance feature \mathbf{f}_i . Rather than employing random initialization that would lack intrinsic spatial correlation, we construct these

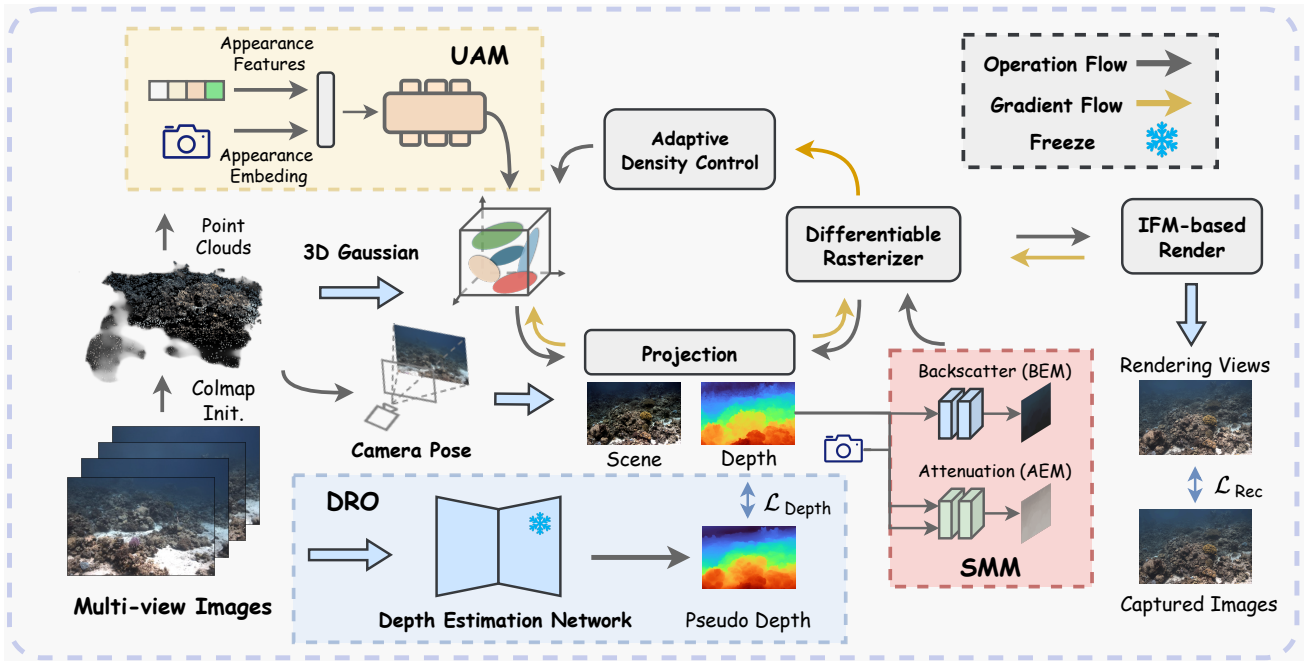


Fig. 2. Overview of the proposed method. Our method disentangles object appearance from water medium effects through specialized Gaussian modeling. **Underwater Appearance Modeling (UAM)** branch incorporates appearance features and embeddings to handle view consistency challenges. **Scatter Medium Modeling (SMM)** branch separately models backscatter and attenuation. **Depth-guided Regularization Optimization (DRO)** uses pseudo-depth maps to improve parameter estimation. All components integrate through a physics-based underwater image formation model during differentiable rasterization.

features using multi-scale Fourier encoding to establish a locality-preserving prior:

$$\mathbf{f}_i = \text{Concat}\{\sin(\pi p_k 2^m), \cos(\pi p_k 2^m)\}, \quad (9)$$

where point coordinates p_k (for $k \in \{1, 2, 3\}$) are normalized to $[0, 1]$ using the 0.97 quantile of the L^∞ norm, with m ranging from 1 to 4, following the setting in [52].

Our complete appearance modeling framework uses a parameterized function \mathcal{F}_θ to synthesize the image-conditioned color by combining the base Gaussian color c_i , appearance feature \mathbf{f}_i , and view-specific embedding \mathbf{e}_j :

$$\hat{c}_i = \mathcal{F}_\theta(c_i, \mathbf{f}_i, \mathbf{e}_j). \quad (10)$$

This integrated methodology enables our model to maintain a consistent appearance across diverse viewpoints while effectively modeling the complex color variations inherent in underwater environments, significantly enhancing both novel view synthesis quality and physical plausibility.

B. Scatter Medium Modeling

Underwater scenes exhibit floating artifacts from backscatter, which intensifies with distance independent of scene content. Recent methods [7], [18], [47] employ Neural Water Fields to implicitly estimate medium parameters through point-based features and radiance MLPs. However, this implicit approach suffers from initialization sensitivity and increased computational complexity due to viewpoint-conditioned MLPs, while their pixel-wise parameter estimations neglect the fundamental distance-dependent distribution of underwater light transport parameters.

To address these limitations, we propose a depth-guided explicit scene medium modeling approach that decomposes underwater medium effects into backscatter and attenuation estimations. Unlike the implicit mappings used in recent neural methods or the linear fitting procedures adopted by Sea-thru [15], our framework introduces a lightweight, learning-based approach that explicitly models scattering media. Built upon the physical principles of Sea-thru, the architecture of our **Scatter Medium Modeling** framework is illustrated in Fig. 3. This physically principled approach enhances the representation capacity for complex underwater light transport phenomena through a fully convolutional structure that directly processes depth information to optimize medium parameters [53]. In comparison to the traditional MLP-based or linear fitting optimization approaches, our method significantly reduces computational complexity while maintaining high efficiency.

For backscatter estimation, we formulate the backscatter intensity \hat{B}_c based on Sea-thru IFM [15] for color channel c as:

$$\hat{B}_c = B_c^\infty (1 - \exp(-b \cdot z)) + B_c^{res} \exp(-d \cdot z), \quad (11)$$

where B_c^∞ denotes the asymptotic backscatter intensity at infinite distance, b represents the backscatter accumulation rate, z corresponds to the distance in water, and B_c^{res} and d are modulation parameters that characterize near-distance backscatter behavior. To efficiently implement this physics-based model, we employ convolutional operations to process the rendered depth map D , enabling direct estimation of the relevant optical parameters. The parameters are computed through 2D convolutional layers to generate the coefficients b

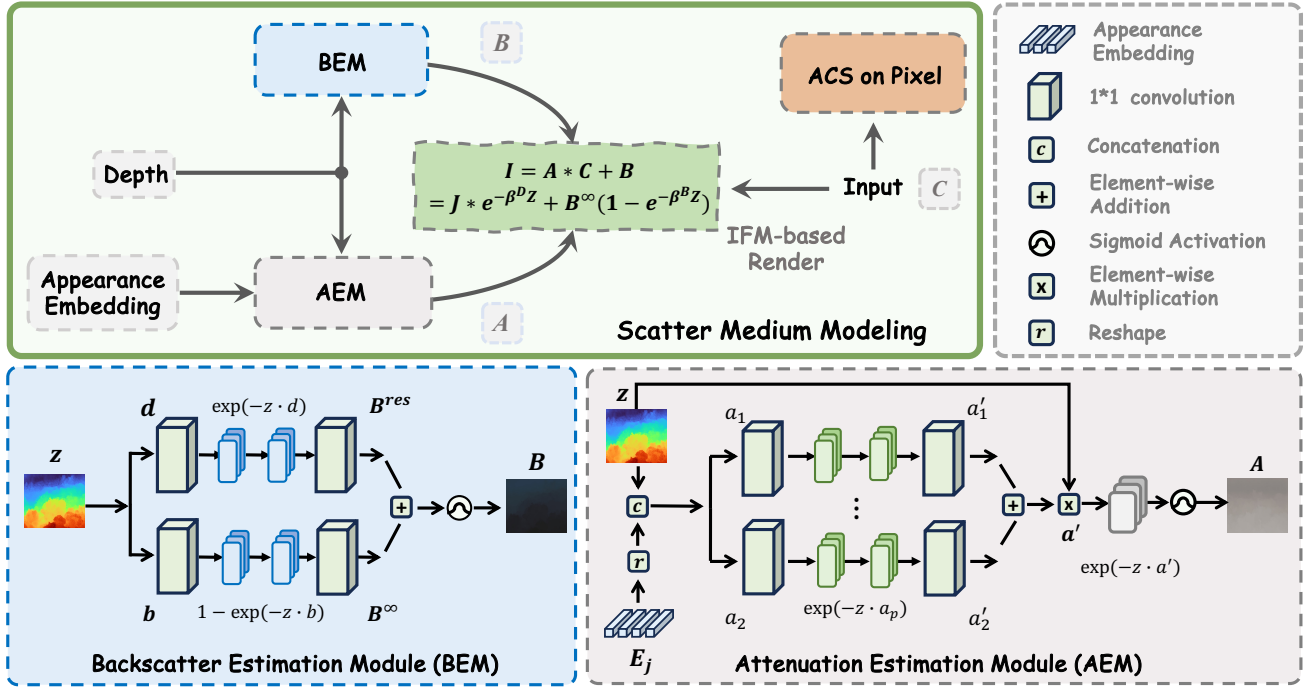


Fig. 3. The top illustrates an overview of the proposed **Scatter Medium Modeling** framework, which decomposes underwater medium effects based on a physical imaging model. The bottom presents the detailed architectures of the **Backscatter Estimation Module (BEM)** and the **Attenuation Estimation Module (AEM)**, respectively. The BEM computes the backscatter component, while the AEM estimates the attenuation coefficients of the direct component, effectively modeling the complex light transport in underwater environments.

and d for each color channel, which allows these parameters to be optimized through gradient descent during training.

For attenuation estimation, we utilize an exponential function to approximate the attenuation coefficient $a_c(z)$ for each color channel [15]:

$$a_c(z) = \sum_{p=1}^P a_c^{p'} \exp(-z \cdot a_c^p), \quad (12)$$

where $a_c^{p'} \in [0, 1]$, and P represent the number of exponential functions used to approximate the complex wavelength-dependent attenuation, respectively.

To mitigate dependency on initial parameter values and enhance robustness, we incorporate depth information and appearance embedding e as initialization context for medium parameter estimation. Specifically, we concatenate the depth map D with the appearance embedding e_j from our UAM branch to construct a comprehensive representation of scene characteristics:

$$z' = \text{Concat}(D, e_j). \quad (13)$$

After estimating the medium parameters, our comprehensive underwater image formation model integrates both appearance color \hat{C} and medium properties through a physics-based formulation. Through the joint optimization of this model, we can simultaneously obtain the reconstructed underwater image and recover the true color without water effects following Eq (6):

$$I_c = \underbrace{a_c(z) \cdot \hat{C}_c}_{\text{Direct}} + \underbrace{\hat{B}_c}_{\text{Backscatter}}. \quad (14)$$

The rendered restored image C represents colors corrected along the depth direction. Depending on the imaging geometry,

this intermediate result may require additional correction to achieve color characteristics equivalent to those of an image captured at the sea surface [15]. General underwater restoration approaches [15], [39] employ global or local white balancing post-processing on the restored image J to normalize color distribution and improve visual appearance. Similar to these underwater image restoration works, we apply adaptive contrast stretching (ACS) on the rendered image C to avoid color oversaturation. The mapping process is formulated as:

$$I_{tm}^c = (I^c - I_{\min}^c) \frac{I_{\max}^o - I_{\min}^o}{I_{\max}^c - I_{\min}^c}, \quad (15)$$

where I_{\max}^o and I_{\min}^o define the target stretching ranges, as measured by the Gray-world hypothesis [54], ensuring optimal color balance and contrast enhancement.

By leveraging rendered depth maps for medium parameter optimization and incorporating physical constraints into the 3D Gaussian representation, we effectively disentangle water effects from object appearance, significantly reducing floating artifacts while enhancing cross-view consistency and physical accuracy in underwater 3D reconstruction.

C. Reconstruction Optimization

Our underwater 3D GS framework employs reconstruction loss (\mathcal{L}_c), depth regularization loss (\mathcal{L}_d), and underwater scale regularization loss (\mathcal{L}_s) to reconstruct complex underwater scenes. The overall loss function \mathcal{L} is defined as:

$$\mathcal{L} = \mathcal{L}_c + \mathcal{L}_d + \mathcal{L}_s. \quad (16)$$

For the reconstruction loss, we adopt the approach from vanilla 3DGS [6], which combines L1 loss and D-SSIM loss to optimize the 3D Gaussian parameters:

$$\mathcal{L}_c = (1 - \lambda_1)\mathcal{L}_1 + \lambda_1\mathcal{L}_{D\text{-SSIM}}, \quad (17)$$

where $\lambda_1 = 0.2$ is the respective weight to balance the contributions from the L1 loss and D-SSIM loss.

For the medium model, precise depth information is crucial for accurately representing underwater scenes. We utilize DepthAnythingV2 [55], a robust monocular depth estimation model, to generate pseudo ground truth depth maps D' . We transform our depth map to its inverse form $D = 1/(\mathcal{D} + 1)$, and compute the L1 loss between rendered and pseudo depths.

While the pseudo depth provides overall depth structure, direct rendering of depth using Eq. (5) can lead to artifacts, particularly at object boundaries where depth discontinuities naturally occur. The discrete nature of 3D Gaussians and their finite extent can introduce spurious depth variations that compromise the quality of novel view synthesis. To address this issue while preserving legitimate depth discontinuities, we introduce an edge-aware depth smoothness regularization term that adapts its strength based on local image content:

$$\mathcal{L}_{DS} = \frac{1}{P} \sum_{p=1}^P \left| \frac{\nabla D_p(\phi)}{\max(\nabla I_p(\phi), \gamma)} \right|, \quad (18)$$

where ∇ represents the first-order spatial derivative operator encompassing both horizontal (∇_x) and vertical (∇_y) gradients, I denotes the rendering image (treated as a constant during backpropagation), $P = H \times W$ represents the total number of pixels, and γ is a small regularization constant to prevent numerical instability from division by zero. This regularization uses image gradients to guide depth changes, enforcing smoothness only in regions where the image intensity changes significantly (i.e., edges or texture areas), while allowing more flexibility in depth changes in flatter regions of the image.

Additionally, in regions far from the camera's line of sight, foreground and background objects may appear similar in color despite having significantly different depths. In such cases, the smoothness term may over-regularize depth variations at true boundaries, resulting in the loss of important geometric details. To complement the edge-aware term and ensure robust boundary preservation, we incorporate anisotropic total variation (TV) regularization:

$$\mathcal{L}_{DC} = \text{mean}(|\nabla_x D|) + \text{mean}(|\nabla_y D|), \quad (19)$$

where ∇_x and ∇_y are spatial gradients in the directions of x and y , respectively.

By summarizing all depth-related supervision and regularization terms, we define the complete depth loss function as:

$$\mathcal{L}_d = \lambda_2 \|D - D'\|_1 + \lambda_3 \mathcal{L}_{DS} + \lambda_4 \mathcal{L}_{DC}, \quad (20)$$

where we set $\lambda_2 = 0.1$, $\lambda_3 = 0.01$, and $\lambda_4 = 0.1$.

In underwater scene reconstruction, volumetric semi-transparent water medium complicates accurate surface modeling. General 3D GS generates Gaussian centers p_i positioned throughout these translucent volumes rather than adhering to solid surfaces, making them unsuitable for direct surface

reconstruction in underwater environments. We apply scale regularization to refine the 3D Gaussian ellipsoids into highly flat shapes, reducing interference from the semi-transparent medium [57]. This process narrows the Gaussians significantly, pulling their centers closer to actual physical surfaces while minimizing water volume representation. Specifically, we penalize the minimal scaling component of each Gaussian:

$$\mathcal{L}_s = \lambda_5 \|\min(s_1, s_2, s_3)\|_1, \quad (21)$$

where $\lambda_5 = 100$, s_1 , s_2 , and s_3 are the scaling parameters of each Gaussian ellipsoid. Minimizing \mathcal{L}_s effectively collapses the shortest axis of each ellipsoid, compressing Gaussians into surface-tangent discs. This regularization suppresses volumetric water interference while concentrating Gaussian centers near physical surfaces, enabling clear disambiguation between water medium and solid surfaces during reconstruction.

V. EXPERIMENTS

A. Experimental Settings

Datasets. We evaluate our method on three datasets: SeaThru-NeRF [7], Underwater in the Wild (U-IW) [56], and our Simulated Underwater dataset (S-U). SeaThru-NeRF contains four forward-facing real underwater scenes with diverse aquatic and imaging conditions. It encapsulates a wide range of water conditions and imaging scenarios, with unbounded camera-to-scene distances. U-IW comprises densely sampled frames from in-the-wild underwater videos collected from the Internet. The dataset includes more complete camera trajectories, often covering 360° views around underwater scenes. This provides richer temporal and spatial cues, enabling more comprehensive evaluations under general real-world conditions. To further evaluate our method, we simulated underwater scenes using four scenes from the MipNeRF-360 dataset [58]. The construction follows the setup described in [7]. The water range is determined from depth maps predicted by 3DGS with gsplat [59]. Following the setup in [7], underwater scenarios are simulated according to Eq. (6) with parameter values $\beta^D = [1.3, 1.2, 0.9]$, $\beta^B = [0.95, 0.85, 0.7]$, and $B^\infty = [0.07, 0.2, 0.39]$. All scenes are preprocessed with COLMAP [49] to extract camera poses and initialize Gaussian positions from sparse point clouds.

Implementations. We adopt hyperparameter values from [6] and train all scenes for 30k iterations. The scene modeling with one MLP contains three linear layers with 128 hidden units. We adopt the densification strategy of AbsGS [23]. We employ the Adam optimizer with a learning rate of 10^{-3} for MLP training. All experiments are conducted on an NVIDIA RTX 3090 GPU.

Baselines and Metrics. We compare our method with several representative baselines retrained under the same setting, including vanilla 3DGS [6], Splatfacto-W (in the wild) [60], and recent underwater NVS methods such as SeaThru-NeRF [15] (implemented on Nerfstudio [61]), RecGS [45], SeaSplat [19], and Water-Splatting [18]. For each baseline method, we assess rendering quality using PSNR, SSIM, and LPIPS.

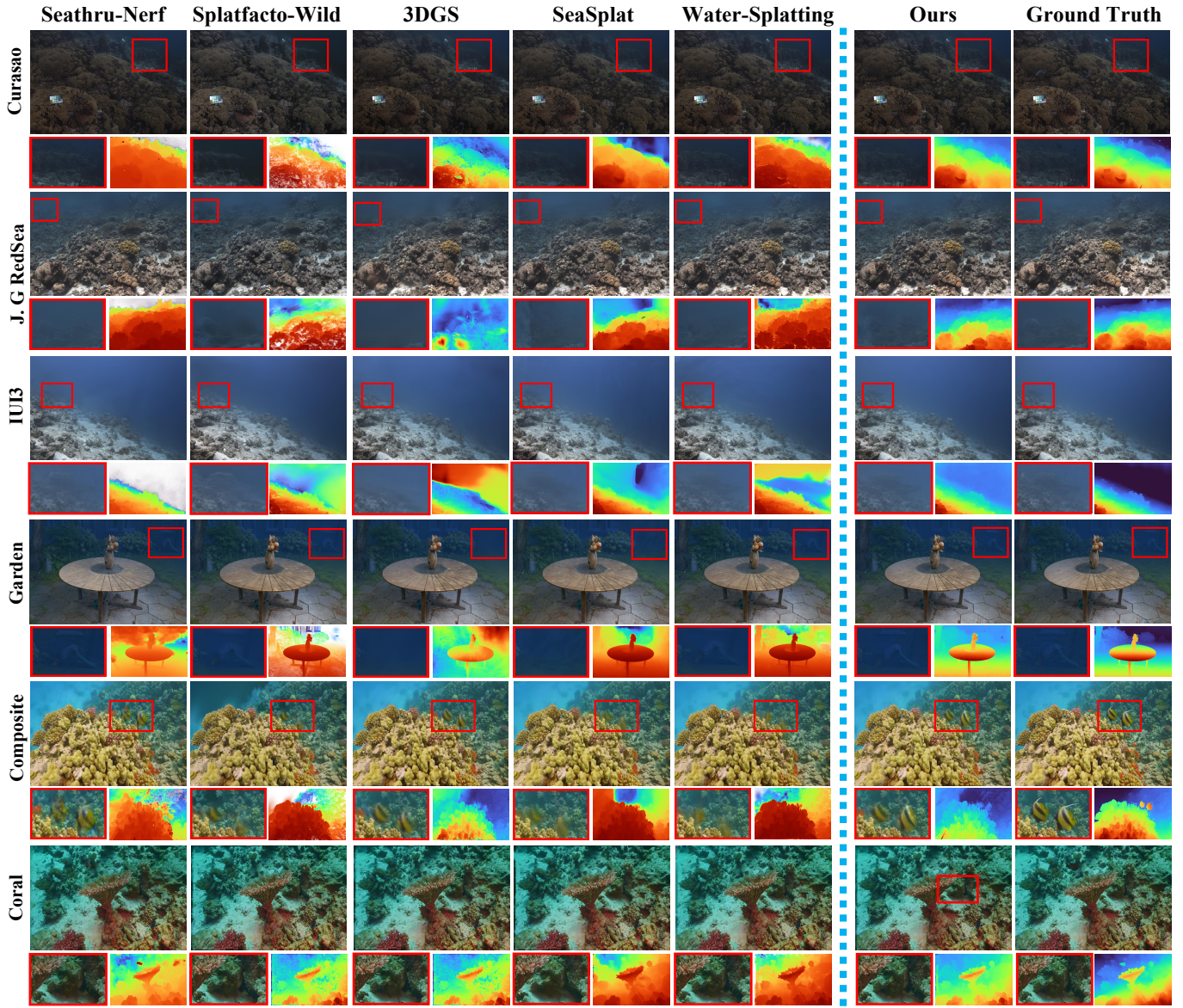


Fig. 4. Qualitative comparison of underwater NVS tasks on real-world and simulated datasets. We visualize the rendered depth maps and zoomed-in scene details. The proposed method outperforms other approaches in capturing scene details and maintaining scene consistency, whereas other methods exhibit floating artifacts and inaccurate depth estimation (*Zoom-in for best view*).

TABLE I

QUANTITATIVE EVALUATION OF EXISTING METHODS. METRICS ARE AVERAGED ACROSS ALL SCENES IN VARIOUS DATASETS. THE TOP THREE RANKINGS IN EACH CATEGORY ARE HIGHLIGHTED: 1ST, 2ND AND 3RD. ARROWS INDICATE WHETHER HIGHER (↑) OR LOWER (↓) VALUES ARE BETTER.

	Seathru-Nerf			U-IW			S-U			Speed	
	PSNR ↑	SSIM ↑	LPIPS ↓	PSNR ↑	SSIM ↑	LPIPS ↓	PSNR ↑	SSIM ↑	LPIPS ↓	FPS ↑	Training Time ↓
SeaThru-Nerf [7]	27.394	0.860	0.215	18.942	0.644	0.383	24.436	0.805	0.293	0.55	2 h 39 m
3DGS [6]	26.188	0.859	0.238	27.361	0.894	0.158	29.274	0.881	0.233	149.36	17 m
Splatfacto-Wild [60]	25.750	0.832	0.229	25.159	0.847	0.209	25.786	0.853	0.260	42.98	21 m
SeaSplat [19]	27.385	0.866	0.194	27.023	0.889	0.159	28.566	0.861	0.253	42.69	1 h 25 m
RecGS [45]	25.829	0.857	0.233	22.186	0.838	0.180	24.620	0.825	0.259	146.62	38 m
Water-Splatting [18]	27.573	0.865	0.198	25.673	0.882	0.167	29.973	0.878	0.235	35.80	29 m
Ours	28.116	0.876	0.202	28.198	0.902	0.150	31.227	0.891	0.187	48.72	48 m

B. Experimental Results

Reconstruction Quality. Fig. 4 suggests that our method achieves superior reconstruction quality by effectively mit-

igating the effects of water-column artifacts and providing coherent depth estimation. In particular, for the geometry reconstruction, the enhanced detail recovery is most notice-

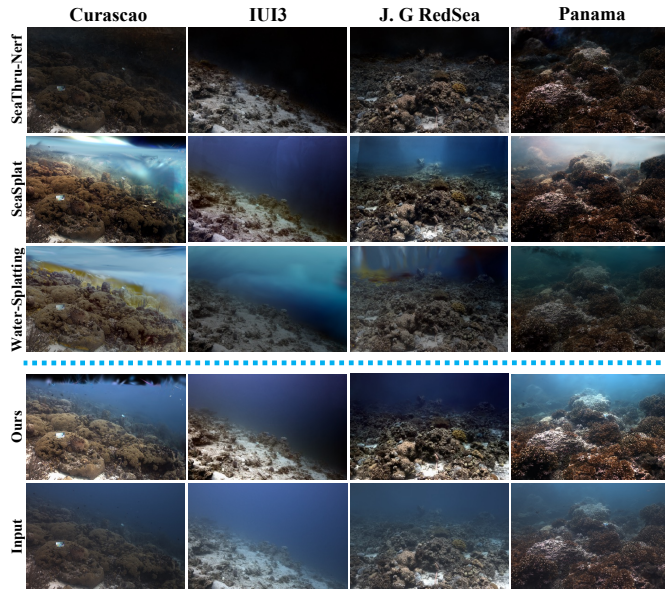


Fig. 5. Visualization of novel view restoration on the Seathru-NeRF Dataset [7]. Our method achieves superior restoration quality with impressive visibility and scene consistency compared to other underwater NVS methods.

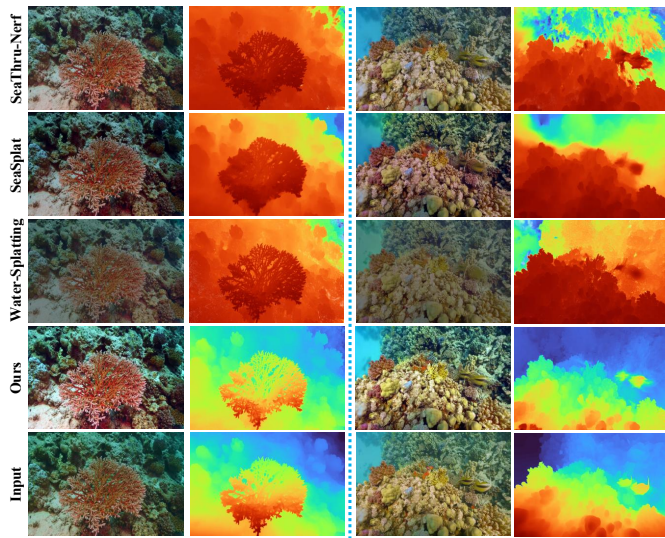


Fig. 6. Visualization of novel view restoration on the U-IW Dataset [56]. Our method achieves superior restoration quality with accurate exposure balance across diverse scenes, outperforming other underwater NVS methods.

able, which mitigates the effects of water-specific artifacts that plague underwater imaging. While alternative approaches exhibit obvious floating artifacts and inaccurate distant scene reconstruction, our method maintains coherent scene structure throughout the water column. This is particularly evident in the Coral and Composite scenes, where complex underwater structures are preserved with significantly higher fidelity. Furthermore, our approach ensures a more accurate and consistent depth map, where other methods exhibit floating artifacts and collapsed depth issues, especially in complex underwater environments. The inconsistent depth estimations and blurry scene details are caused by water-specific artifacts, which often hinder accurate underwater reconstruction in other methods.

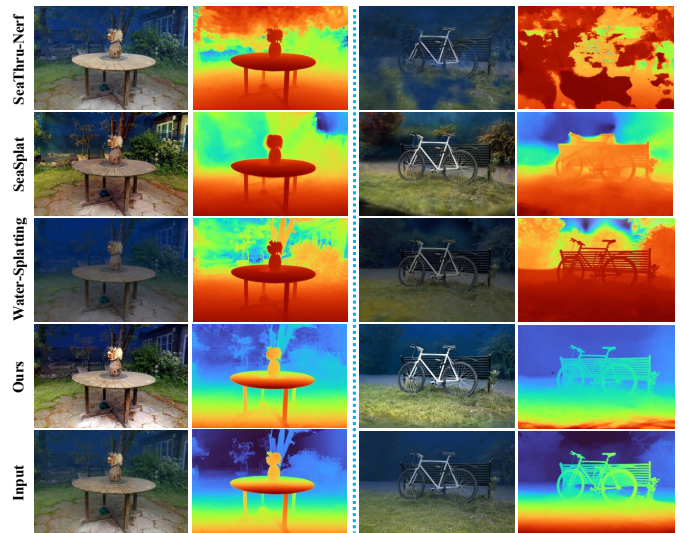


Fig. 7. Visualization of novel view restoration on the U-S Dataset. Our method achieves superior restoration quality, particularly excelling in the preservation of depth details compared to other underwater NVS methods.

The visual consistency observed across all tested datasets further demonstrates the robustness of our method in real-world underwater scenarios, where water conditions and scene complexities vary greatly. This consistency is particularly important when dealing with diverse aquatic environments, as our approach adapts to different underwater conditions with minimal loss in reconstruction quality. Overall, the results show that our method excels in both scene restoration quality and depth estimation, leading to more realistic underwater scene representations and accurate scene geometry.

Scene Restoration. Figs. 5, 6, and 7 present the scene restoration results for novel views. 3DGS [6], Splatfacto-Wild [60], and RecGS [45] lack medium modeling in their rendering pipelines, thus failing to achieve effective de-scattering restoration and are excluded from these comparisons. For these visual results of scene restoration, our method achieves superior quality by enhancing underwater visibility and preserving structural and temporal consistency more effectively than existing NVS methods. The visual enhancements are most prominent in the accurate preservation of scene depth and structure, where our approach outperforms others in terms of global scene restoration. Specifically, the proposed appearance modeling and depth-guided optimization contribute to more natural and coherent background restorations, especially in distant regions. The depth-aware representation ensures that both foreground and background elements are restored with appropriate spatial relationships, further enhancing the realism of the restored scene. Additionally, the 2D white balance during the rendering process ensures a more natural appearance across varying illumination conditions and further enhances the visual realism of the restored views.

Furthermore, we provide an interactive comparison web demo on our [project page](#) for additional visual results. This demo offers dynamic visual support for comprehensive cross-method evaluation, enabling real-time toggling between RGB renderings, depth estimations, and descattering-enhanced

TABLE II

QUANTITATIVE RESULTS: RESULTS ON FOUR REAL-WORLD UNDERWATER SCENES FROM THE SEATHRU-NERF DATASET [7]: CURASCAO, IUI3-REDSEA, J. G REDSEA, AND PANAMA. EVALUATION METRICS (PSNR/SSIM/LPIPS) DEMONSTRATE THE EFFECTIVENESS OF DIFFERENT SCENE RECONSTRUCTION METHODS, WITH TOP THREE RANKINGS IN EACH CATEGORY ARE HIGHLIGHTED: 1ST, 2ND AND 3RD.

	Curacao			IUI3-RedSea			J. G RedSea			Panama		
	PSNR (rank)	SSIM (rank)	LPIPS (rank)	PSNR (rank)	SSIM (rank)	LPIPS (rank)	PSNR (rank)	SSIM (rank)	LPIPS (rank)	PSNR (rank)	SSIM (rank)	LPIPS (rank)
SeaThru-Nerf [7]	30.870 (2)	0.891 (6)	0.222 (7)	26.748 (4)	0.824 (5)	0.281 (4)	23.213 (3)	0.844 (3)	0.193 (3)	28.747 (4)	0.881 (4)	0.162 (1)
3DGS [6]	29.601 (6)	0.893 (4)	0.220 (6)	24.912 (6)	0.826 (4)	0.290 (6)	21.316 (7)	0.835 (5)	0.223 (6)	28.921 (2)	0.884 (3)	0.217 (7)
Splatfacto-Wild [60]	28.048 (7)	0.876 (7)	0.209 (4)	25.697 (5)	0.806 (7)	0.292 (7)	22.962 (4)	0.815 (7)	0.204 (5)	26.291 (7)	0.829 (6)	0.210 (6)
SeaSplat [19]	30.768 (3)	0.898 (3)	0.186 (2)	27.493 (3)	0.832 (2)	0.213 (1)	22.698 (5)	0.845 (2)	0.196 (4)	28.580 (5)	0.887 (2)	0.180 (4)
RecGS [45]	29.313 (6)	0.893 (4)	0.211 (5)	24.363 (7)	0.823 (6)	0.289 (5)	21.812 (6)	0.834 (6)	0.224 (7)	27.829 (6)	0.879 (7)	0.208 (5)
Water-Splatting [18]	30.583 (4)	0.904 (2)	0.174 (1)	27.593 (2)	0.831 (3)	0.275 (3)	23.363 (2)	0.845 (2)	0.178 (1)	28.751 (3)	0.881 (4)	0.163 (2)
Ours	30.978 (1)	0.907 (1)	0.187 (3)	28.301 (1)	0.841 (1)	0.252 (2)	23.371 (1)	0.857 (1)	0.187 (2)	29.816 (1)	0.900 (1)	0.181 (3)

TABLE III

QUANTITATIVE RESULTS: RESULTS ON FOUR IN-THE-WILD UNDERWATER SCENES FROM THE U-IW DATASET [56]: TURTLE, CORAL, SARDINE AND COMPOSITE. EVALUATION METRICS (PSNR/SSIM/LPIPS) DEMONSTRATE THE EFFECTIVENESS OF DIFFERENT SCENE RECONSTRUCTION METHODS, WITH TOP THREE RANKINGS IN EACH CATEGORY ARE HIGHLIGHTED: 1ST, 2ND AND 3RD.

	Turtle			Coral			Sardine			Composite		
	PSNR (rank)	SSIM (rank)	LPIPS (rank)	PSNR (rank)	SSIM (rank)	LPIPS (rank)	PSNR (rank)	SSIM (rank)	LPIPS (rank)	PSNR (rank)	SSIM (rank)	LPIPS (rank)
SeaThru-Nerf [7]	13.067 (7)	0.542 (7)	0.502 (8)	25.354 (7)	0.855 (7)	0.160 (6)	13.893 (7)	0.383 (7)	0.624 (7)	23.456 (6)	0.795 (7)	0.248 (7)
3DGS [6]	32.145 (3)	0.958 (2)	0.112 (2)	28.432 (2)	0.907 (1)	0.114 (2)	22.797 (2)	0.838 (4)	0.247 (4)	26.071 (3)	0.874 (2)	0.158 (3)
Splatfacto-Wild [60]	28.324 (4)	0.929 (4)	0.158 (5)	25.788 (6)	0.868 (6)	0.162 (7)	19.941 (5)	0.766 (5)	0.286 (5)	26.585 (2)	0.826 (6)	0.232 (6)
SeaSplat [19]	32.294 (2)	0.957 (3)	0.107 (1)	27.595 (4)	0.895 (5)	0.124 (5)	22.703 (3)	0.839 (3)	0.241 (3)	25.500 (5)	0.864 (5)	0.165 (5)
RecGS [45]	24.836 (6)	0.875 (6)	0.116 (3)	25.970 (5)	0.904 (3)	0.115 (4)	15.343 (6)	0.708 (6)	0.330 (6)	22.596 (7)	0.866 (4)	0.162 (4)
Water-Splatting [18]	26.075 (5)	0.912 (5)	0.174 (6)	28.225 (3)	0.902 (4)	0.113 (1)	22.666 (4)	0.843 (2)	0.237 (2)	25.727 (4)	0.873 (3)	0.146 (1)
Ours	32.538 (1)	0.959 (1)	0.117 (4)	28.735 (1)	0.907 (1)	0.114 (2)	24.974 (1)	0.867 (1)	0.218 (1)	26.546 (2)	0.877 (1)	0.153 (2)

TABLE IV

QUANTITATIVE RESULTS: RESULTS ON FOUR SYNTHETIC 360 SCENES FROM THE S-U DATASET [58]: GARDEN, BICYCLE, STUMP, AND COUNTER. EVALUATION METRICS (PSNR/SSIM/LPIPS) DEMONSTRATE THE EFFECTIVENESS OF DIFFERENT SCENE RECONSTRUCTION METHODS, WITH TOP THREE RANKINGS IN EACH CATEGORY ARE HIGHLIGHTED: 1ST, 2ND AND 3RD.

	Garden			Bicycle			Stump			Counter		
	PSNR (rank)	SSIM (rank)	LPIPS (rank)	PSNR (rank)	SSIM (rank)	LPIPS (rank)	PSNR (rank)	SSIM (rank)	LPIPS (rank)	PSNR (rank)	SSIM (rank)	LPIPS (rank)
SeaThru-Nerf [7]	26.024 (7)	0.884 (7)	0.188 (3)	22.391 (7)	0.730 (7)	0.361 (7)	25.110 (5)	0.738 (6)	0.364 (7)	24.221 (6)	0.867 (6)	0.259 (7)
3DGS [6]	32.515 (2)	0.922 (2)	0.191 (4)	28.136 (3)	0.856 (2)	0.242 (3)	25.497 (4)	0.808 (3)	0.320 (3)	30.947 (2)	0.937 (2)	0.178 (2)
Splatfacto-Wild [60]	27.140 (6)	0.894 (6)	0.224 (7)	24.491 (5)	0.814 (6)	0.280 (5)	22.747 (6)	0.774 (5)	0.335 (5)	28.765 (5)	0.928 (3)	0.201 (3)
SeaSplat [19]	30.524 (4)	0.896 (5)	0.209 (6)	27.896 (4)	0.836 (3)	0.258 (4)	26.531 (3)	0.800 (4)	0.320 (3)	29.312 (4)	0.911 (5)	0.225 (5)
RecGS [45]	27.416 (5)	0.899 (4)	0.207 (5)	26.144 (6)	0.831 (4)	0.237 (2)	22.649 (7)	0.745 (7)	0.335 (5)	22.270 (7)	0.826 (7)	0.256 (6)
Water-Splatting [18]	31.897 (3)	0.922 (2)	0.175 (2)	28.381 (2)	0.829 (5)	0.280 (5)	29.097 (1)	0.837 (1)	0.279 (2)	30.517 (3)	0.925 (4)	0.208 (4)
Ours	33.203 (1)	0.923 (1)	0.142 (1)	30.253 (1)	0.875 (1)	0.181 (1)	28.975 (2)	0.832 (2)	0.255 (1)	32.475 (1)	0.934 (1)	0.171 (1)

results across different approaches.

Quantitative Evaluations. Table I presents the average metrics across all dataset scenes, while Tables II, III, and IV provide per-scene metric tables detailing quantitative evaluations across all test scenarios. For quantitative results, our method consistently outperforms state-of-the-art approaches across three challenging datasets. We achieve the highest PSNR and SSIM values while maintaining low LPIPS scores on three datasets. The per-scene evaluation scores further reveal our method maintains this performance advantage consistently across diverse underwater scenes, from unbounded to surround scenes and from simple to complex underwater scene geometries. Notably, our method performs well in challenging scenarios, even when optimal LPIPS scores are not achieved in certain scenes. This trade-off highlights the inherent challenges in underwater scene reconstruction, where improvements in one visual quality aspect may sometimes compromise another. Nevertheless, our approach achieves the best balance across all metrics when considered holistically, prioritizing accurate scene reconstruction while maintaining competitive perceptual quality. These comparison results highlight the effectiveness of

our approach in handling underwater scene degradation and reconstructing high-fidelity visual content.

Rendering Efficiency. Table I shows rendering speed and training time across four Seathru-Nerf scenes. Our method achieves faster rendering and training than SeaThru-Nerf despite the latter’s Nerfstudio acceleration. While our scene-medium modeling and depth optimization introduce slight computational overhead compared to vanilla 3DGS, we maintain real-time rendering with superior visual quality among underwater media methods, demonstrating an effective balance between reconstruction fidelity and efficiency.

C. Ablation Study

We conduct ablation studies on the Seathru-Nerf datasets with results averaged across all scenes in Figs. 8, 9 and Table V. Our experiments validate the effectiveness of three key modules. The scene disentanglement strategy shows significant improvements over the baseline 3DGS model when adding SMM and UAM separately. The medium model enhances accurate representation of underwater media by reducing floating artifacts caused by translucent medium occlusion

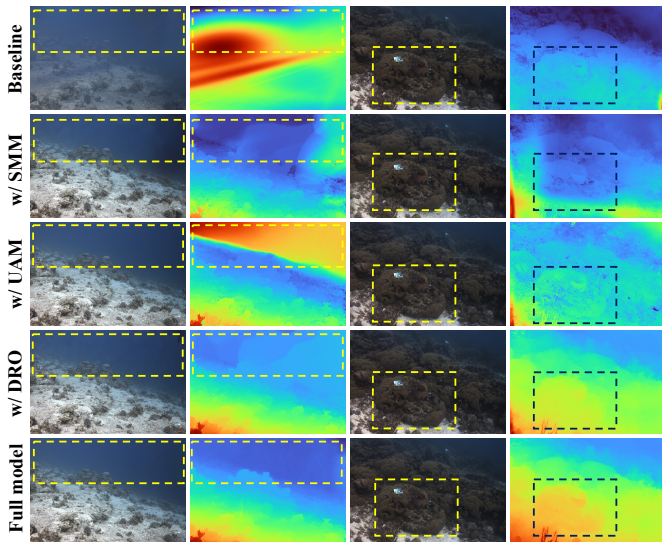


Fig. 8. Visualization of ablation studies on different components. Depth maps better illustrate medium modeling effects. Highlighted regions (dashed boxes) reveal progressive improvements in detail preservation and consistency across model variants.

while enabling scene restoration capabilities. Meanwhile, the appearance model improves color representation balance and achieves consistent brightness restoration across viewpoints. Further performance gains are achieved when combining both components. This synergistic integration demonstrates that explicit modeling of both intrinsic scene properties and water-induced effects is essential for accurate reconstruction. Among optimization strategies, DRO yields substantial improvement, confirming that explicit depth supervision effectively mitigates volumetric artifacts in challenging underwater scenes. Various loss combinations provide additional refinement when integrated with the core components. Our full model achieves the best performance across all metrics, demonstrating the effectiveness of our comprehensive framework for underwater scene reconstruction.

Furthermore, we also analyze the restored water-free scenes to validate the effectiveness of the final pixel-based white balance. As shown in Fig. 9, incorporating pixel-based white balance during training leads to better restoration, avoiding over- and under-restoration. Additionally, it does not affect the critical geometric accuracy during GS training, as evidenced by the nearly identical visual results in Fig. 9 and the closely matched metrics in Table V, which demonstrates its effectiveness in complex real-world scenarios.

VI. CONCLUSION

This paper addresses two critical issues in underwater scene representation: floating artifacts from incorrectly modeled water volumes and inconsistent appearance across viewpoints due to wavelength-dependent attenuation. To achieve that, we propose a physics-based 3DGS framework that explicitly models complex underwater light transport. Our method disentangles scene representation into object appearance and medium components, effectively overcoming standard volume rendering limitations in underwater scattering media. Through learned

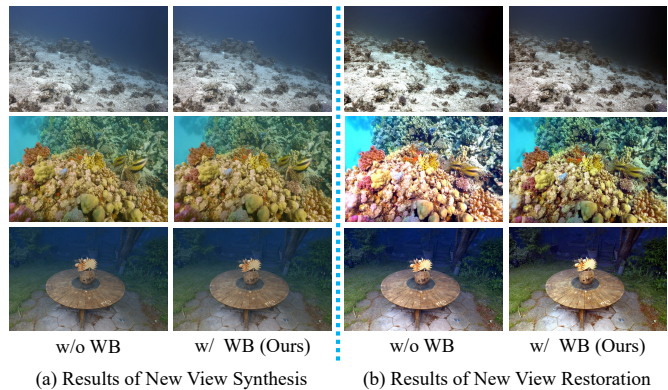


Fig. 9. Visualization of ablation studies on white balance. (a): novel view synthesis results demonstrate that pixel-based white balance does not disturb geometry reconstruction; (b): the corresponding restored views show that white balance achieves more visually balanced restorations by avoiding both over-enhancement and under-restoration.

TABLE V
ABLATION STUDY RESULTS FOR EVALUATING THE CONTRIBUTION OF EACH COMPONENT TO THE OVERALL PERFORMANCE. LOSS EXPERIMENTS ARE CONDUCTED ON THE SMM+UAM FOUNDATION.

Method	PSNR \uparrow	SSIM \uparrow	LPIPS \downarrow
Baseline	26.188	0.859	0.238
only w/ Medium (SMM)	26.698	0.864	0.216
only w/ Appearance (UAM)	27.245	0.867	0.210
only w/ Depth Optimization (DRO)	26.769	0.861	0.215
SMM \mathcal{L}_c	27.507	0.868	0.209
+ $\mathcal{L}_c + \mathcal{L}_d$	27.839	0.874	0.205
UAM $\mathcal{L}_c + \mathcal{L}_s$	27.691	0.867	0.211
w/o Pixel based White Balance (ACS)	28.083	0.876	0.203
Ours (Full Model)	28.116	0.877	0.202

embeddings for view-dependent variations and depth-guided optimization with specialized Gaussian flattening constraints, our method achieves more natural viewpoint variations and accurate depth estimation. Experiments show our method achieves the state-of-the-art novel view synthesis quality with real-time physically accurate scene restoration. The ability of aquatic scene precise representation and restoration expands the possibilities for subsequent underwater view synthesis enhancement.

REFERENCES

- [1] F. Zhang, S. You, Y. Li, and Y. Fu, “Atlantis: Enabling underwater depth estimation with stable diffusion,” in *Proc. IEEE Conf. Comput. Vis. Pattern Recog.*, Jun. 2024, pp. 11 852–11 861.
- [2] J. Yuan, Z. Cai, and W. Cao, “A novel underwater detection method for ambiguous object finding via distraction mining,” *IEEE Trans. Ind. Inform.*, vol. 20, no. 7, pp. 9215–9224, Apr. 2024.
- [3] J. Zhou, Z. He, D. Zhang, S. Liu, X. Fu, and X. Li, “Spatial residual for underwater object detection,” *IEEE Trans. Pattern Anal. Mach. Intell.*, vol. 47, no. 6, pp. 4996–5013, Mar. 2025.
- [4] M. Yuval and T. Treibitz, “Releasing a dataset of 3d models of artificial reefs from the northern red-sea for 3d printing and virtual reality applications,” *Remote Sens. Appl. Soc. Environ.*, vol. 36, p. 101305, Nov. 2024.

- [5] W. Wang, B. Joshi, N. Burgdorfer, K. Batsosc, A. Q. Lid, P. Mordohaia, and I. Rekleitib, “Real-time dense 3d mapping of underwater environments,” in *Proc. IEEE Int. Conf. Robot. Autom.*, Jul. 2023, pp. 5184–5191.
- [6] B. Kerbl, G. Kopanas, T. Leimkühler, and G. Drettakis, “3D gaussian splatting for real-time radiance field rendering,” *ACM Trans. Graph.*, vol. 42, no. 4, pp. 1–14, Jul. 2023.
- [7] D. Levy, A. Peleg, N. Pearl, D. Rosenbaum, D. Akkaynak, S. Korman, and T. Treibitz, “SeaThru-NeRF: Neural radiance fields in scattering media,” in *Proc. IEEE Conf. Comput. Vis. Pattern Recog.*, Jun. 2023, pp. 56–65.
- [8] J. S. Jaffe, “Computer modeling and the design of optimal underwater imaging systems,” *IEEE J. Ocean. Eng.*, vol. 15, no. 2, pp. 101–111, Apr. 1990.
- [9] B. McGlamery, “A computer model for underwater camera systems,” in *Proc. SPIE*, vol. 208, Jan. 1979, pp. 221–231.
- [10] D. Akkaynak, T. Treibitz, T. Shlesinger, Y. Loya, R. Tamir, and D. Iluz, “What is the space of attenuation coefficients in underwater computer vision?” in *Proc. IEEE Conf. Comput. Vis. Pattern Recog.*, Jul. 2017.
- [11] Y. Zhang, J. Yuan, and Z. Cai, “DCGF: Diffusion-color-guided framework for underwater image enhancement,” *IEEE Trans. Geosci. Remote Sens.*, vol. 63, pp. 1–12, 2025.
- [12] B. Mildenhall, P. P. Srinivasan, M. Tancik, J. T. Barron, R. Ramamoorthi, and R. Ng, “NeRF: Representing scenes as neural radiance fields for view synthesis,” in *Proc. Eur. Conf. Comput. Vis.*, Nov. 2020.
- [13] W.-T. Chen, W. Yifan, S.-Y. Kuo, and G. Wetzstein, “DehazeNeRF: Multi-image haze removal and 3d shape reconstruction using neural radiance fields,” in *Proc. Int. Conf. 3D Vis.*, Jun. 2024, pp. 247–256.
- [14] D. Akkaynak, T. Treibitz, T. Shlesinger, Y. Loya, R. Tamir, and D. Iluz, “What is the space of attenuation coefficients in underwater computer vision?” in *Proc. IEEE Conf. Comput. Vis. Pattern Recog.*, Jul. 2017, pp. 568–577.
- [15] D. Akkaynak and T. Treibitz, “Sea-Thru: A method for removing water from underwater images,” in *Proc. IEEE Conf. Comput. Vis. Pattern Recog.*, Jun. 2019.
- [16] R. Martin-Brualla, N. Radwan, M. S. M. Sajjadi, J. T. Barron, A. Dosovitskiy, and D. Duckworth, “Nerf in the wild: Neural radiance fields for unconstrained photo collections,” in *Proc. IEEE Conf. Comput. Vis. Pattern Recog.*, Jun. 2021, pp. 7210–7219.
- [17] B. Lee, H. Lee, X. Sun, U. Ali, and E. Park, “Deblurring 3d gaussian splatting,” in *Proc. Eur. Conf. Comput. Vis.*, Jun. 2024.
- [18] H. Li, W. Song, T. Xu, A. Elsig, and J. Kulhanek, “Watersplating: Fast underwater 3d scene reconstruction using gaussian splatting,” in *Proc. Int. Conf. 3D Vis.*, 2025.
- [19] D. Yang, J. J. Leonard, and Y. Girdhar, “SeaSplat: Representing underwater scenes with 3d gaussian splatting and a physically grounded image formation model,” in *Proc. IEEE Int. Conf. Robot. Autom.*, 2025.
- [20] J. T. Barron, B. Mildenhall, M. Tancik, P. Hedman, R. Martin-Brualla, and P. P. Srinivasan, “Mip-NeRF: A multiscale representation for anti-aliasing neural radiance fields,” in *Proc. Int. Conf. Comput. Vis.*, Oct. 2021, pp. 5855–5864.
- [21] T. Müller, A. Evans, C. Schied, and A. Keller, “Instant neural graphics primitives with a multiresolution hash encoding,” *ACM Trans. Graph.*, vol. 41, no. 4, Jul. 2022.
- [22] Z. Yu, A. Chen, B. Huang, T. Sattler, and A. Geiger, “Mip-Splatting: Alias-free 3d gaussian splatting,” in *Proc. IEEE Conf. Comput. Vis. Pattern Recog.*, June 2024, pp. 19447–19456.
- [23] Z. Ye, W. Li, S. Liu, P. Qiao, and Y. Dou, “Absgs: Recovering fine details in 3d gaussian splatting,” in *Proc. ACM Int. Conf. Multimedia*, 2024.
- [24] B. Mildenhall, P. Hedman, R. Martin-Brualla, P. P. Srinivasan, and J. T. Barron, “Nerf in the dark: High dynamic range view synthesis from noisy raw images,” in *Proc. IEEE Conf. Comput. Vis. Pattern Recog.*, Jun. 2022, pp. 16190–16199.
- [25] Y. Cai, Z. Xiao, Y. Liang, M. Qin, Y. Zhang, X. Yang, Y. Liu, and A. Yuille, “HDR-GS: Efficient high dynamic range novel view synthesis at 1000x speed via gaussian splatting,” in *Proc. Adv. Neural Inform. Process. Syst.*, 2024.
- [26] X. Jin, P. Jiao, Z.-P. Duan, X. Yang, C.-L. Guo, B. Ren, and C. Li, “Lighting every darkness with 3dgs: Fast training and real-time rendering for hdr view synthesis,” in *Proc. Adv. Neural Inform. Process. Syst.*, 2024.
- [27] H. Dahmani, M. Bennehar, N. Piasco, L. Roldão, and D. Tsishkou, “SWAG: Splatting in the wild images with appearance-conditioned gaussians,” in *Proc. Eur. Conf. Comput. Vis.*, Oct 2024, pp. 325–340.
- [28] D. Zhang, C. Wang, W. Wang, P. Li, M. Qin, and H. Wang, “Gaussian in the wild: 3d gaussian splatting for unconstrained image collections,” in *Proc. Eur. Conf. Comput. Vis.*, Jun. 2024, pp. 341–359.
- [29] Y.-T. Peng and P. C. Cosman, “Underwater image restoration based on image blurriness and light absorption,” *IEEE Trans. Image Process.*, vol. 26, no. 4, pp. 1579–1594, 2017.
- [30] Y.-T. Peng, K. Cao, and P. C. Cosman, “Generalization of the dark channel prior for single image restoration,” *IEEE Trans. Image Process.*, vol. 27, no. 6, pp. 2856–2868, Feb. 2018.
- [31] J. Yuan, Z. Cai, and W. Cao, “TEBCF: Real-world underwater image texture enhancement model based on blurriness and color fusion,” *IEEE Trans. Geosci. Remote Sens.*, vol. 60, pp. 1–15, Oct. 2022.
- [32] C. Li, S. Anwar, J. Hou, R. Cong, C. Guo, and W. Ren, “Underwater image enhancement via medium transmission-guided multi-color space embedding,” *IEEE Trans. Image Process.*, vol. 30, pp. 4985–5000, May 2021.
- [33] Z. Wang, L. Shen, M. Xu, M. Yu, K. Wang, and Y. Lin, “Domain adaptation for underwater image enhancement,” *IEEE Trans. Image Process.*, vol. 32, pp. 1442–1457, Feb. 2023.
- [34] Y. Rao, W. Liu, K. Li, H. Fan, S. Wang, and J. Dong, “Deep color compensation for generalized underwater image enhancement,” *IEEE Trans. Circuits Syst. Video Technol.*, vol. 34, no. 4, pp. 2577–2590, Apr. 2024.
- [35] Z. Wang, L. Shen, Y. Yu, and Y. Hui, “Uierl: Internal-external representation learning network for underwater image enhancement,” *IEEE Trans. Multimedia*, vol. 26, pp. 9252–9267, Apr. 2024.
- [36] W. Zhang, Q. Liu, H. Lu, J. Wang, and J. Liang, “Underwater image enhancement via wavelet decomposition fusion of advantage contrast,” *IEEE Trans. Circuits Syst. Video Technol.*, pp. 1–1, 2025.
- [37] D. Akkaynak and T. Treibitz, “A revised underwater image formation model,” in *Proc. IEEE Conf. Comput. Vis. Pattern Recog.*, Jun. 2018.
- [38] Z. Liang, X. Ding, Y. Wang, X. Yan, and X. Fu, “GUDCP: Generalization of underwater dark channel prior for underwater image restoration,” *IEEE Trans. Circuits Syst. Video Technol.*, vol. 32, no. 7, pp. 4879–4884, Jul. 2022.
- [39] R. Cong, W. Yang, W. Zhang, C. Li, C.-L. Guo, Q. Huang, and S. Kwong, “PUGAN: Physical model-guided underwater image enhancement using gan with dual-discriminators,” *IEEE Trans. Image Process.*, vol. 32, pp. 4472–4485, Jun. 2023.
- [40] S. Yan, X. Chen, Z. Wu, M. Tan, and J. Yu, “Hybrur: A hybrid physical-neural solution for unsupervised underwater image restoration,” *IEEE Trans. Image Process.*, vol. 32, pp. 5004–5016, Sep. 2023.
- [41] O. B. Nathan, D. Levy, T. Treibitz, and D. Rosenbaum, “Osmosis: Rgb-diffusion prior for underwater image restoration,” in *Proc. Eur. Conf. Comput. Vis.*, Oct. 2024, pp. 302–319.
- [42] X. Guo, Y. Dong, X. Chen, W. Chen, Z. Li, F. Zheng, and C.-M. Pun, “Underwater image restoration via polymorphic large kernel cnns,” in *Proc. IEEE Int. Conf. Acoust. Speech Signal Process.*, 2025, pp. 1–5.
- [43] C. Boittiaux, R. Marxer, C. Dune, A. Arnaubec, M. Ferrera, and V. Hugel, “SUCRe: Leveraging scene structure for underwater color restoration,” in *Proc. Int. Conf. 3D Vis.*, 2024.
- [44] J. Zhou, T. Liang, D. Zhang, S. Liu, J. Wang, and E. Q. Wu, “WaterHE-NeRF: Water-ray matching neural radiance fields for underwater scene reconstruction,” *Inf. Fusion*, p. 102770, Mar. 2024.
- [45] T. Zhang, W. Zhi, B. Meyers, N. Durrant, K. Huang, J. Mangelson, C. Barbalata, and M. Johnson-Roberson, “Recgs: Removing water caustic with recurrent gaussian splatting,” *IEEE Robot. Autom. Lett.*, vol. 10, no. 1, pp. 668–675, Jan. 2025.
- [46] N. Muallem, R. Amoyal, O. Freifeld, and D. Akkaynak, “Gaussian Splashing: Direct volumetric rendering underwater,” arXiv preprint arXiv:2411.19588, 2024. [Online]. Available: <https://arxiv.org/abs/2411.19588>
- [47] H. Wang, N. Anantrasirichai, F. Zhang, and D. Bull, “UW-GS: Distractor-aware 3d gaussian splatting for enhanced underwater scene reconstruction,” in *Proc. IEEE Winter Conf. Appl. Comput. Vis.*, Feb. 2025.
- [48] S. Liu, J. Lu, Z. Gu, J. Li, and Y. Deng, “Aquatic-GS: A hybrid 3d representation for underwater scenes,” arXiv preprint arXiv:2411.00239, 2025. [Online]. Available: <https://arxiv.org/abs/2411.00239>
- [49] J. L. Schonberger and J.-M. Frahm, “Structure-from-motion revisited,” in *Proc. IEEE Conf. Comput. Vis. Pattern Recog.*, Jun. 2016.
- [50] G. Fang and B. Wang, “Mini-Splatting: Representing scenes with a constrained number of gaussians,” in *Proc. Eur. Conf. Comput. Vis.*, Oct. 2024.
- [51] T. Wen, Z. Liu, B. Lu, and Y. Fang, “Scaffold-SLAM: Structured 3d gaussians for simultaneous localization and photorealistic mapping,”

- arXiv preprint arXiv:2501.05242, 2025. [Online]. Available: <https://arxiv.org/abs/2501.05242>
- [52] J. Kulhanek, S. Peng, Z. Kukulova, M. Pollefeys, and T. Sattler, “WildGaussians: 3D gaussian splatting in the wild,” in *Proc. Adv. Neural Inform. Process. Syst.*, 2024.
 - [53] S. Jamieson, J. P. How, and Y. Girdhar, “DeepSeeColor: Realtime adaptive color correction for autonomous underwater vehicles via deep learning methods,” in *Proc. IEEE Int. Conf. Robot. Autom.*, Jul. 2023, pp. 3095–3101.
 - [54] J. Yuan, W. Cao, Z. Cai, and B. Su, “An underwater image vision enhancement algorithm based on contour bougie morphology,” *IEEE Trans. Geosci. Remote Sens.*, vol. 59, no. 10, pp. 8117–8128, Oct. 2021.
 - [55] L. Yang, B. Kang, Z. Huang, Z. Zhao, X. Xu, J. Feng, and H. Zhao, “Depth anything v2,” in *Proc. Adv. Neural Inform. Process. Syst.*, vol. 37. Curran Associates, Inc., 2024, pp. 21 875–21 911.
 - [56] Y. Tang, C. Zhu, R. Wan, C. Xu, and B. Shi, “Neural underwater scene representation,” in *Proc. IEEE Conf. Comput. Vis. Pattern Recog.*, Jun. 2024, pp. 11 780–11 789.
 - [57] D. Chen, H. Li, W. Ye, Y. Wang, W. Xie, S. Zhai, N. Wang, H. Liu, H. Bao, and G. Zhang, “PGSR: Planar-based gaussian splatting for efficient and high-fidelity surface reconstruction,” *IEEE Trans. Vis. Comput. Graph.*, pp. 1–12, Nov. 2024.
 - [58] J. T. Barron, B. Mildenhall, D. Verbin, P. P. Srinivasan, and P. Hedman, “Mip-NeRF 360: Unbounded anti-aliased neural radiance fields,” in *Proc. IEEE Conf. Comput. Vis. Pattern Recog.*, Jun. 2022, pp. 5470–5479.
 - [59] V. Ye, R. Li, J. Kerr, M. Turkulainen, B. Yi, Z. Pan, O. Seiskari, J. Ye, J. Hu, M. Tancik, and A. Kanazawa, “gsplat: An open-source library for gaussian splatting,” arXiv preprint arXiv:2409.06765, 2024. [Online]. Available: <https://arxiv.org/abs/2409.06765>
 - [60] C. Xu, J. Kerr, and A. Kanazawa, “Splatfacto-W: A nerfstudio implementation of gaussian splatting for unconstrained photo collections,” arXiv preprint arXiv:2407.12306, 2024. [Online]. Available: <https://arxiv.org/abs/2407.12306>
 - [61] M. Tancik, E. Weber, E. Ng, R. Li, B. Yi, J. Kerr, T. Wang, A. Kristoffersen, J. Austin, K. Salahi, A. Ahuja, D. McAllister, and A. Kanazawa, “Nerfstudio: A modular framework for neural radiance field development,” in *Proc. ACM SIGGR.*, 2023.